Highlights

Can the anisotropic hydraulic conductivity of an aquifer be determined using surface displacement data? A case study

Sona Salehian Ghamsari, Tonie van Dam, Jack S. Hale

- We explore the potential utility of InSAR displacement data for inferring information about anisotropic conductivity in aquifer systems.
- We develop a three-dimensional finite element model mimicking the main features of the 1994 Anderson Junction pumping test.
- Hydraulic anisotropic behaviour leads to subsidence patterns with distinctive elliptical shape.
- Recommendations for pumping test design are made with respect to the inherent constraints when acquiring InSAR data.

Can the anisotropic hydraulic conductivity of an aquifer be determined using surface displacement data? A case study

Sona Salehian Ghamsari [a,*], Tonie van Dam [b], Jack S. Hale [a]

[a] *Institute of Computational Engineering, Department of Engineering, Faculty of Science, Technology, and Medicine, University of Luxembourg, 6 avenue de la Fonte, Esch-sur-Alzette, L-4364, Luxembourg*

[b] *Department of Geology and Geophysics, College of Mines and Earth Sciences, University of Utah, 201 Presidents' Cir, Salt Lake City, 84112-0102, Utah, United States*

Abstract

Due to geological features such as fractures, some aquifers demonstrate strongly anisotropic hydraulic behavior. The goal of this study is to use a poroelastic model to calculate surface displacements given known pumping rates to predict the potential utility of Interferometric Synthetic Aperture Radar (InSAR) data for inferring information about anisotropic hydraulic conductivity (AHC) in aquifer systems. To this end, we develop a three-dimensional anisotropic poroelastic model mimicking the main features of the 1994 Anderson Junction aquifer test in southwestern Utah with a 24 to 1 ratio of hydraulic conductivity along the principal axes, previously estimated in the literature using traditional well observation techniques. Under suitable model assumptions, our results show that anisotropy in the hydraulic problem leads to a distinctive elliptical surface displacement pattern centered around the pumping well that could be detected with InSAR. We interpret these results in the context of InSAR acquisition constraints and provide guidelines for designing future pumping tests so that InSAR data can be used to its full potential for improving the characterization of aquifers with anisotropic hydraulic behavior.

Keywords: anisotropic hydraulic conductivity, poroelasticity, aquifer

*Corresponding author

Email addresses: `salehiyan.sona@gmail.com` (Sona Salehian Ghamsari), `tonie.vandam@utah.edu` (Tonie van Dam), `mail@jackhale.co.uk` (Jack S. Hale)

systems, InSAR, finite element method.

---

1. Introduction

Groundwater is a vital resource that provides drinking water to billions of people and supports critical agriculture and industrial activities (Food and Agriculture Organization of the United Nations (FAO), 2022). One of the biggest challenges for sustainability of global groundwater resources is overexploitation (Basu and Van Meter, 2014; Caretta et al., 2022). The consequences of overexploitation include reducing the amount of water available to surface water bodies (Walker et al., 2020), lowering the water table to the extent that it leads to surface subsidence (Heilweil and Hsieh, 2006; Burbey et al., 2006; Galloway and Burbey, 2011) and saltwater intrusion (Guo et al., 2019b). Over-exploitation of groundwater resources is a global issue with the largest impacts in areas with high population densities, rapid urbanization and agricultural intensification (Poland, 1984; Famiglietti et al., 2011; Erkens et al., 2015).

Consequently, there is a need for increased research and monitoring to understand better the complex hydrological processes that govern groundwater systems and contribute data to support effective management strategies. To this end, groundwater modeling and simulation tools have become an increasingly important component in supporting decision-makers to design effective strategies (Singh, 2014; Amitrano et al., 2014). One aspect of ensuring that groundwater simulation tools can produce reasonable predictions is ensuring that all possible data sources are assimilated into the model for e.g. parameter inference. Specifically, in this study, we ask "is there potentially valuable information in Interferometric Synthetic Aperture Radar (InSAR) data for inferring anisotropic hydraulic conductivity (AHC) in a poroelastic model of an aquifer?". This question forms part of broader research efforts on developing new approaches for assimilating remote sensing data into hydrogeomechanical models of aquifers – however, we do not tackle the data assimilation problem here.

The use of InSAR in hydrogeological research has become increasingly popular due to its high precision in measuring ground surface displacement, wide-area coverage and cost-effectiveness (Guzy and Malinowska, 2020; Galloway and Hoffmann, 2007). InSAR observations of surface uplift and subsidence allow inference of groundwater levels and flow gradients (Gambolati and Teatini, 2015). InSAR observations can be used to determine the structural boundaries of aquifer systems (Chaussard et al., 2014; Haghighi and Motagh, 2019; Hu and Bürgmann, 2020), provide the temporal evolution of the ground surface (Zhou et al., 2018; Guo et al., 2019a; Bonì et al., 2017) and to contribute to estimate storage coefficients and hydraulic conductivity (Hu et al., 2018; Bonì et al., 2016; Chaussard et al., 2014). Development of InSAR technology has contributed to the regional hydrogeological models of groundwater flow and land deformation (Galloway and Hoffmann, 2007; Gambolati and Teatini, 2015). Since the accuracy of the InSAR measurement is the most important parameter for the estimation of the aquifer properties (Guzy and Malinowska, 2020) and using InSAR time-series enhances the accuracy of surface displacement estimation (Li et al., 2022), consequently using InSAR time-series would improve the accuracy of estimating aquifer properties.

The pumping of subsurface fluids during an aquifer test causes a drop in pore pressure which leads to a three-dimensional deformation. This response has been simulated using a number of modeling approaches, see e.g. (Guzy and Malinowska, 2020). While conventional groundwater flow theory in the aquitard drainage model has been widely used (Helm, 1986; Harbaugh et al., 2000; Hoffmann et al., 2003; Harbaugh, 2005) it has been argued that the use of numerical poroelasticity models is necessary for realistic aquifer settings (Hsieh, 1996). The theory of poroelasticity introduced by Biot (1941) describes the interactions between water, the porous matrix of rock and solid grains. This theory explains how changes in pressure and fluid content within the porous matrix can cause deformation and stress among the solid grains, and vice versa. Verruijt (1969) proposed a formulation of Biot's linear theory that is suitable for problems in soil mechanics. In the context of calibrating groundwater flow models with InSAR-derived displacement data, it is necessary to use a model that directly links fluid flow to deformation by including poroelasticity theory.

The underlying cause of AHC in hydrogeology is often a preferential rock fracturing direction that allows for higher fluid conductivity along the direction of fractures (Berre et al., 2019). The recognition of the importance of AHC on the behaviour of aquifer systems dates back to the work of Papadopulos (1965) who presented a method to determine the hydraulic conductivity of a homogeneous anisotropic aquifer from the observation of pressure (head drop) at a minimum of three wells situated at different directions around a constant-rate aquifer extraction test. Heilweil and Hsieh (2006) demonstrated that AHC could be inferred from two observation wells, if the wells are assumed to be aligned with the principal directions of AHC. The possibility was also mentioned by Burbey (2006).

In the specific context of AHC and geodesy, both Burbey et al. (2006) and Burbey (2006) proposed that the elliptical vertical surface displacement pattern observed from Global Positioning System (GPS) receivers positioned around a Nevada pumping test could be directly related to the interaction between an anisotropy in the fluid flow and rock skeleton. In support of this theory, Burbey (2006) presented computer simulations based on a poroelasticity theory showing elliptical vertical displacement patterns at the Earth's surface under a 3 to 1 AHC ratio. The elliptic pattern in the displacements is driven by the underlying anisotropy in the fluid problem caused by the fractures tedency to provide directional conduits for flow.

Galloway and Hoffmann (2007) showed that InSAR can be used to calibrate numerical models of groundwater flow and deformation. Galloway and Burbey (2011) conducted a review of various remote sensing techniques and models used for studying subsidence due to groundwater extraction. Hesse and Stadler (2014) proposed scalable computational methods for assimilating InSAR data into a poroelastic finite element model with spatially varying isotropic hydraulic conductivity within a Bayesian framework. Continuing with the line of work developed by Hesse and Stadler (2014), recently Alghamdi (2020); Alghamdi et al. (2020, 2021) assimilated InSAR data from the test site of Burbey et al. (2006) into a spatially-varying isotropic hydraulic conductivity (IHC) poroelastic model. We remark that in the original study of Burbey et al. (2006) it is mentioned that due to the underlying geology (fracturing) the hydraulic behavior of the site is likely to be strongly anisotropic and therefore the isotropic model used in Alghamdi (2020) for calibration using the data from Burbey et al. (2006) may be insufficient to fully capture the anisotropic behaviour of the site. In addition, the elliptical shape observed in the surface displacement measured by the InSAR technique, as shown in (Alghamdi et al., 2020, Figure 1c), may be evidence of anisotropy, as discussed by Burbey (2006).

In this study, we develop a three-dimensional linear poroelastic model that includes AHC to gain insight into the relationship between surface displacement and pumping at Anderson Junction in southwestern Utah. The goal is to use our anisotropic model to calculate surface displacements given known pumping rates to predict the potential utility of InSAR data for inferring information about AHC in aquifer systems. We choose this site because

Heilweil and Hsieh (2006) specifically studied the role of anisotropy there, giving estimated AHC ratio of around 24 to 1 determined using two observation wells. Using our model, we predict the InSAR Line of Sight (LOS) displacements for the region, i.e. the quantity of interest for calibration of the model against theoretical InSAR observations (Alghamdi, 2020).

We show that the duration of four days and rate of the pumping used in the Anderson Junction test was likely insufficient to induce surface displacements that can be measured with InSAR. We then run our model under a number of alternative scenarios, including different pumping rates, pumping lengths and anisotropy ratios to determine when the displacements would be observable by InSAR. We conclude that there could be pumping regimes in which InSAR data could contain important information about AHC. Finally, we discuss some guidelines for designing future pumping tests in the context of InSAR acquisition constraints.

An outline of this manuscript is as follows. Section 2 provides an overview of the Anderson Junction study area and the aquifer test. In section 3, we outline the theoretical foundations by presenting the Biot equations. In section 4, we introduce the InSAR technique and present the transformation of the three-dimensional deformations into InSAR LOS observations. In section 5, we describe our proposed model in detail. The outcomes of our simulations are presented in section 6. Finally, in section 7 we present the conclusions of our study.

2. Case study

Our case study is located at Anderson Junction, Utah, USA, see fig. 1, and was the subject of the pumping test conducted by the US Geological Survey (USGS) in March and April 1996 to determine the local Navajo Sandstone's anisotropic hydraulic conductivity and storage properties (Heilweil and Hsieh, 2006; Heilweil et al., 2000). The test involved a pumping well `(C-40-13)28dcb-2` and two observation wells, well A, `(C-40-13)28dca-1` and well B, `(C-40-13)28dcc-1` (U.S. Geological Survey, 2016). Groundwater was pumped for approximately 4 days at an average rate of $6000\,\mathrm{m}^3\,\mathrm{d}^{-1}$. Pumping then stopped and well observations continued for 20 days.

The site shown in figs. 2a and 2b features a confined aquifer characterized by a 180 m thick deposit of Navajo sandstone (Heilweil and Hsieh, 2006). The overlying layer consists of unconsolidated mixed alluvial and colluvial

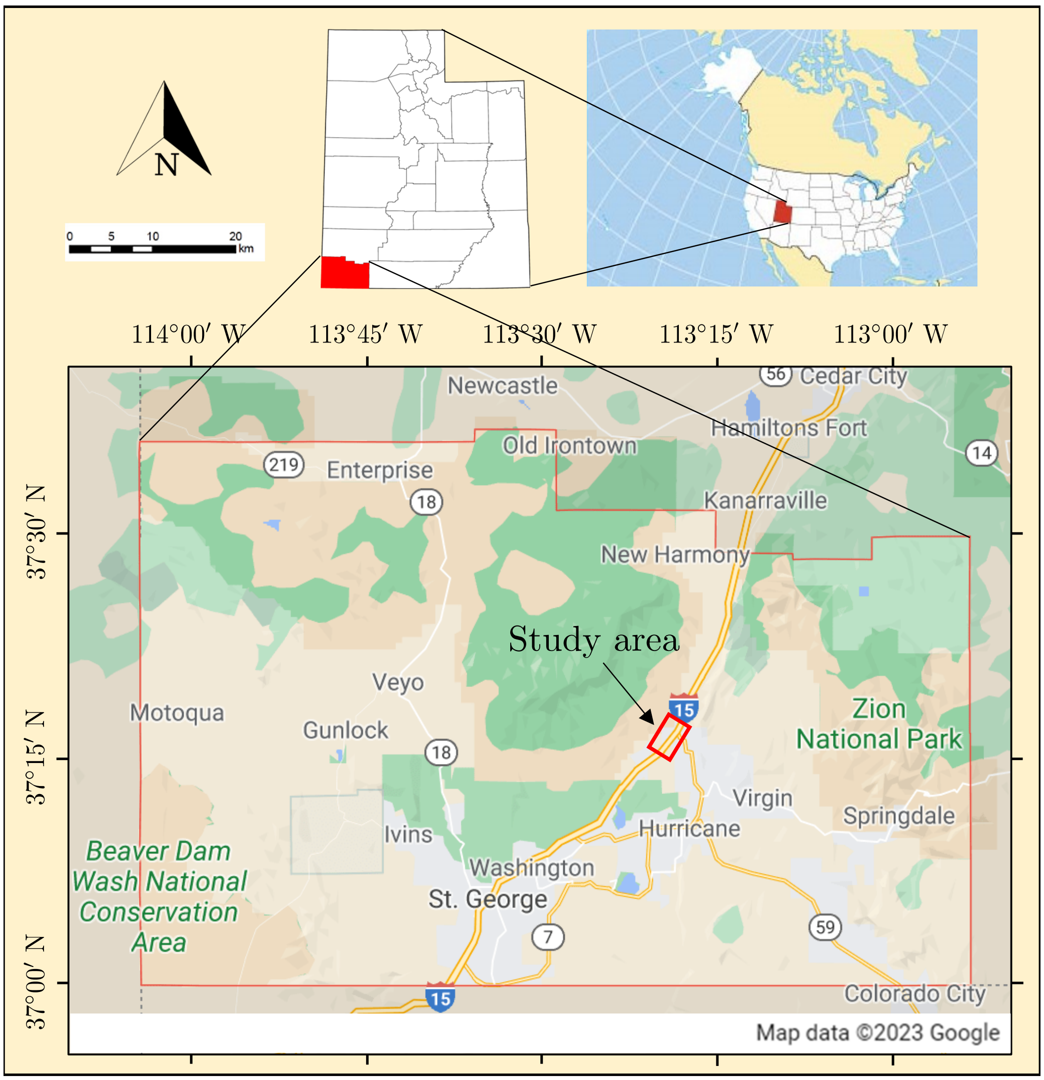

Figure 1: Location of the Anderson Junction site in Utah, USA. Lower map data Copyright Google 2023.

deposits and the underlying layer by the Kayenta formation (Hintze, 1980). The overlying and underlying layers act as confining layers for the aquifer.

The rose diagram Figure 3a shows that the site is strongly characterized by fracturing of the Navajo sandstone, with a primary cluster at 180° to 210°, and a secondary cluster at orientation of 90° to 130°.

The Hurricane Fault and an unnamed series of faults offset the Kayenta Formation and Navajo Sandstone along its length. These faults are assumed to impede groundwater flow perpendicular to their fault planes due to the presence of poorly-sorted breccia and clay-rich materials (Hurlow, 1998).

3. Biot's poroelasticity theory

We describe the three-field formulation of Biot's poroelasticity theory following Ferronato et al. (2010) and Alghamdi (2020). This is used to construct the conceptual model of Anderson Junction in section 5. Full details are given in Appendix A and the code for the solver is included as supplementary material (Salehian Ghamsari and Hale, 2024).

Given a domain $\Omega \subset \mathbb{R}^3$ with boundary Γ and outward-pointing normal n, find the fluid-pore pressure $p : \Omega \times (0, T] \to \mathbb{R}$, deformation $u : \Omega \times (0, T] \to \mathbb{R}^3$ and fluid flux $q : \Omega \times (0, T] \to \mathbb{R}^3$ such that

$$\begin{aligned} (S_\epsilon p + \alpha \nabla \cdot u)_t + \nabla \cdot q &= f_p \text{ on } \Omega \times (0, T], \\ -\nabla \cdot \bar{\sigma}(u, p) &= f_u \text{ on } \Omega \times (0, T], \\ q + k \nabla p &= 0 \text{ on } \Omega \times (0, T], \end{aligned}$$

with notations and units summarised in table 1, plus boundary conditions

$$\begin{aligned} u &= u_d \text{ on } \Gamma_u^d \times (0, T], \\ \bar{\sigma} \cdot n &= g_u \text{ on } \Gamma_u^n \times (0, T], \\ p &= p_d \text{ on } \Gamma_p^d \times (0, T], \\ q \cdot n &= g_p \text{ on } \Gamma_p^n \times (0, T], \end{aligned}$$

where the boundary Γ has been partitioned into disjoint parts for both the solid problem $\Gamma = \Gamma_u^d \cup \Gamma_p^n$ and the fluid problem $\Gamma = \Gamma_p^d \cup \Gamma_p^n$, plus initial conditions

$$\begin{aligned} p(x, 0) &= p^0 \text{ on } \Omega, \\ u(x, 0) &= u^0 \text{ on } \Omega, \\ q(x, 0) &= q^0 \text{ on } \Omega. \end{aligned}$$

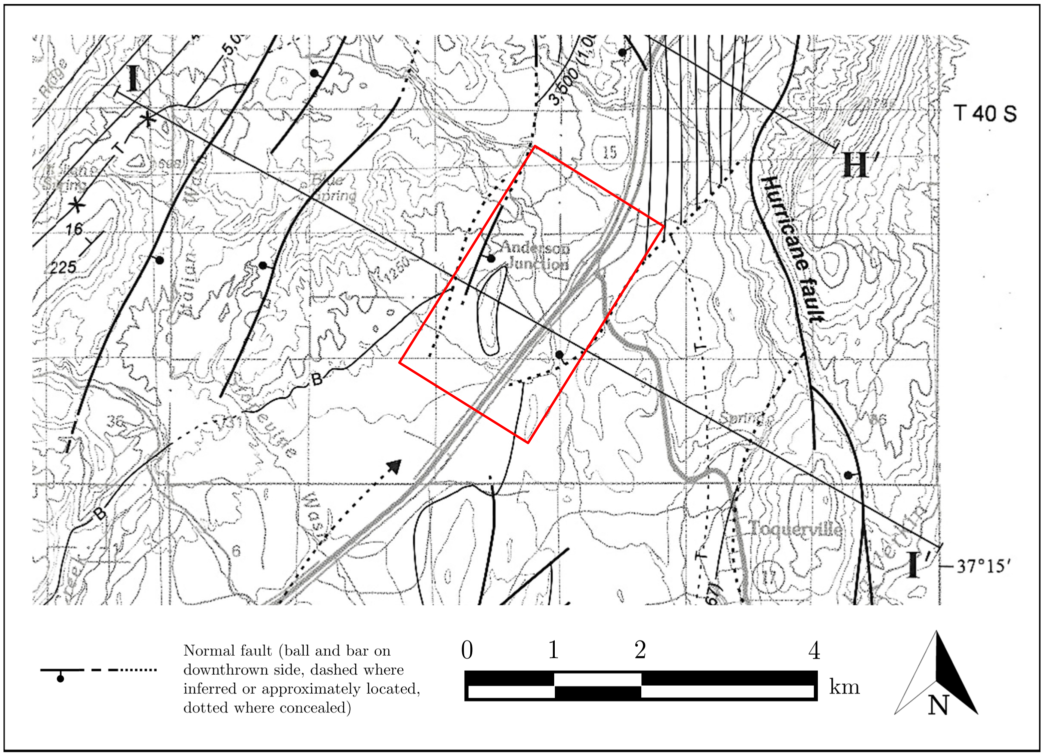

(a) Location of the II’ cross-section transect line on structure-contour map.

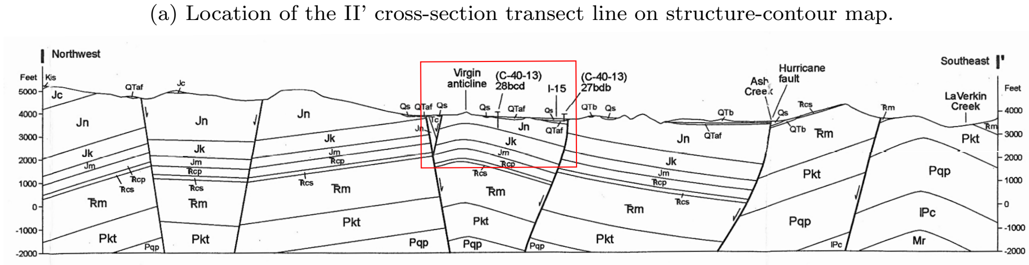

(b) Geologic cross-section of Anderson Junction site.

Figure 2: Geologic cross-section of Anderson Junction site and its location (Image courtesy of U.S. Geological Survey (Hurlow, 1998) in the U.S. Public Domain.). The study area is highlighted by a red rectangle. The y-axis in the cross-section is elevation in feet with respect to mean sea level. The cross-section reveals the geological layers, including the unconsolidated alluvial and colluvial deposits (Qs) on the surface as the upper confining layer, the Navajo sandstone (Jn) as the aquifer layer, and the Kayenta formation (Jk) as the lower confining layer. In the cross-section, faults are depicted as nearly vertical lines. Note that the orientation of the cross-section aligns with the axis of major hydraulic conductivity shown in fig. 3b.

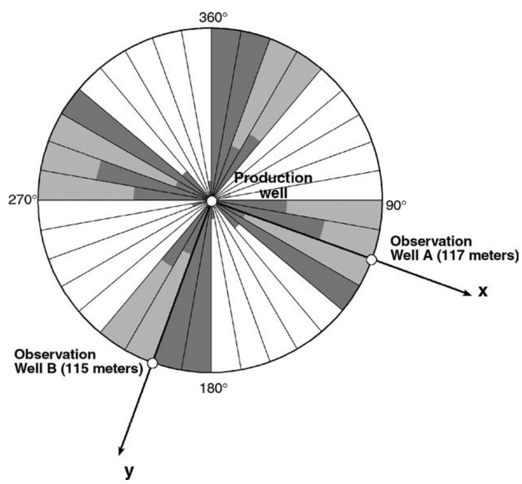

(a) Rose diagram of fracture density

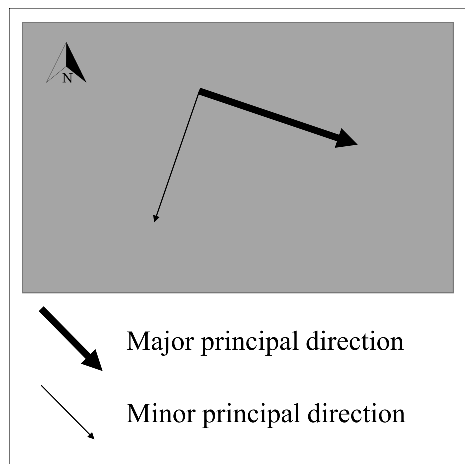

(b) Principal directions of hydraulic conductivity

Figure 3: (a). Rose diagram showing fracture orientations (from Heilweil and Hsieh (2006)) and locations of pumping and observation wells used for the Anderson Junction aquifer test. (b). Principal directions of hydraulic conductivity of the Anderson Junction aquifer system were derived from modified Papadopulos method in Heilweil and Hsieh (2006). Arrows represent major and minor principal directions, indicating that hydraulic conductivity in the major direction is approximately 24 times greater than in the minor direction. Note: Arrow lengths do not signify the scale of hydraulic conductivity.

The AHC is modelled as a second-rank symmetric positive definite tensor. When the principal axis of hydraulic conductivity is aligned with the global coordinate system (x, y, z), this tensor can be represented as a diagonal matrix with positive entries k_{xx}, k_{yy} and k_{zz}

$$k = \begin{bmatrix} k_{xx} & 0 & 0 \\ 0 & k_{yy} & 0 \\ 0 & 0 & k_{zz} \end{bmatrix}.$$

The elastic stress tensor σ is given for isotropic linear elasticity by Hooke's law

$$\sigma = 2\mu_s\varepsilon + \lambda(\mathrm{Tr}\,\varepsilon)I, \tag{1a}$$

$$\varepsilon = \frac{1}{2}\left(\nabla u + (\nabla u)^T\right), \tag{1b}$$

$$\tag{1c}$$

and the Biot stress tensor as

$$\bar{\sigma} = \sigma - \alpha p I, \tag{2}$$

with notations also described in table 1.

4. Calculation and precision of InSAR-derived displacements

The SAR satellite emits radar pulses in the LOS direction, oriented perpendicular to the satellite's direction of motion, see fig. 4. Following (Fuhrmann and Garthwaite, 2019) the displacement in the LOS direction u_{LOS} can be calculated from the incidence angle θ and satellite heading angle α as

$$u_{\mathrm{LOS}} = \begin{bmatrix} -\sin\theta\cos\alpha & \sin\theta\sin\alpha & \cos\theta \end{bmatrix} \begin{bmatrix} u_E \\ u_N \\ u_U \end{bmatrix}. \tag{3}$$

where u_E, u_N, and u_U are deformation in directions of east, north and up, respectively, that can be calculated by transforming the predicted deformation (section 3) in the model coordinate system ($u = (u_x, u_y, u_z)$) to east-north-up (ENU) coordinate system as depicted in Figure 6a. In our calculations, we

Symbol	Description	Units
$()_t$	time derivative	s^{-1}
∇	gradient operator	m^{-1}
$\nabla\cdot$	divergence operator	m^{-1}
Tr	trace operator	dimensionless
$(\cdot)^T$	transpose operator	dimensionless
p	fluid pore pressure	Pa
u	elastic deformation	m
q	volumetric fluid flux	$\mathrm{m\,s^{-1}}$
f_p	fluid source density	s^{-1}
g_p	boundary fluid flux	$\mathrm{m\,s^{-1}}$
f_u	body force density	$\mathrm{N\,m^{-3}}$
g_u	traction	Pa
σ	stress tensor	Pa
$\bar{\sigma}$	Biot stress tensor	Pa
I	identity tensor	dimensionless
α	Biot coefficient	dimensionless
S_ϵ	drained storage coefficient	$\mathrm{Pa^{-1}}$
k	hydraulic conductivity tensor	$\mathrm{m^3\,s\,kg^{-1}}$
μ_s	drained shear modulus	Pa
λ	second Lamé parameter	Pa

Table 1: Table of main notations and units used in the three-field formulation of Biot's poroelasticity theory.

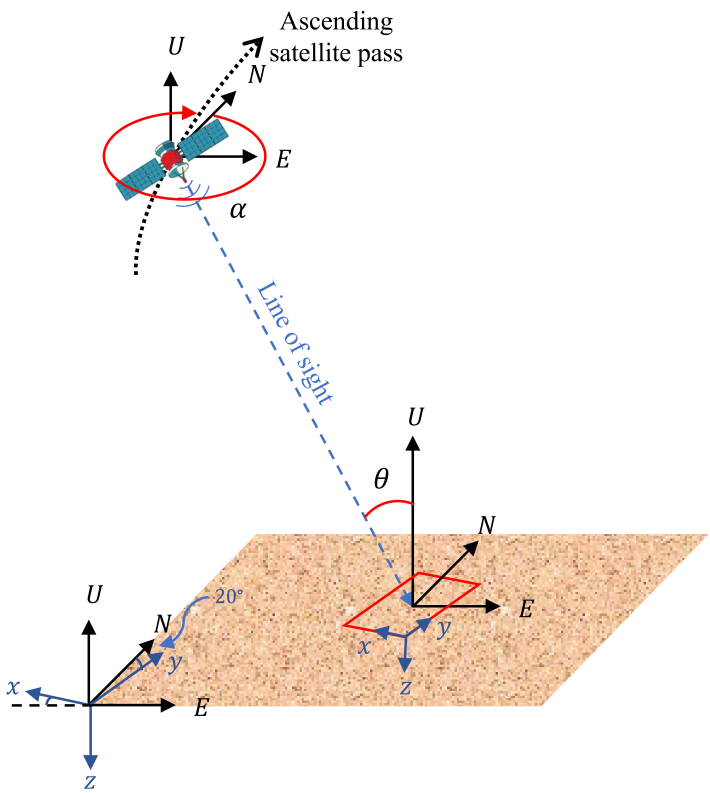

Figure 4: Geometry of Synthetic Aperture Radar (SAR) Imaging showing the incidence angle (θ) and heading angle (α). The study area is highlighted by a red rectangle.

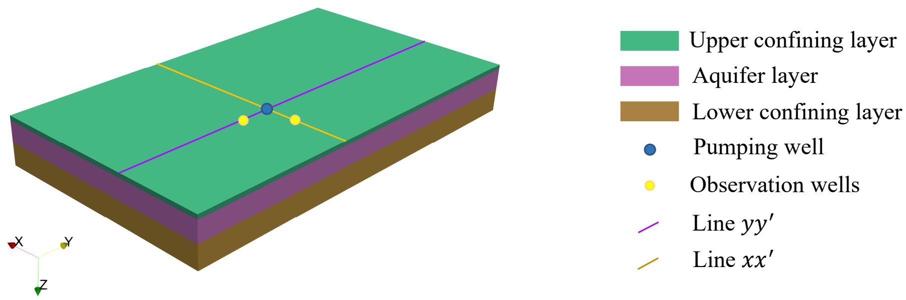

Figure 5: Simulated domain of the aquifer system illustrating the three layers and their element sizes. The figure also highlights the positions of the pumping and observation wells, as well as lines xx' and yy'. The xx' line extends from $x = 0\,\text{m}$ to $x = 2000\,\text{m}$, passing through the pumping well and aligned with the X-axis, while the yy' line extends from $y = 0\,\text{m}$ to $y = 3500\,\text{m}$, also passing through the pumping well and aligned with the Y-axis.

use Sentinel-1 ascending geometry values for a NNW ascending satellite pass taking $\alpha = 15°$ and $\theta = 43.86°$ (European Space Agency (ESA), 2023).

Several studies have shown that achieving sub-centimeter precision using Sentintel-1 is possible (Cigna et al., 2021). For example, comparisons between Sentinel-1 InSAR data and Global Navigation Satellite System (GNSS) measurements reveal a precision of less than 5 mm (Manunta et al., 2019) or 8 mm (Duan et al., 2020). Consequently, when we analyse the results of the simulations in section 6, if the computed LOS is greater than 8 mm we will consider the deformation signal detectable.

5. Conceptual model construction

5.1. Aquifer model layers and parameters

The simulated model domain is shown in fig. 5 with the positions of the pumping and observation wells, along with the xx' and yy' lines that will be used later for extracting results for visualisation.

The three horizontal layers of the aquifer model are shown in fig. 6a – this assumption is made due to a lack of information about the height of layers throughout the aquifer system. The aquifer's width and length were estimated based on the map of effective land subsidence due to groundwater depletion (Herrera-García et al., 2021).

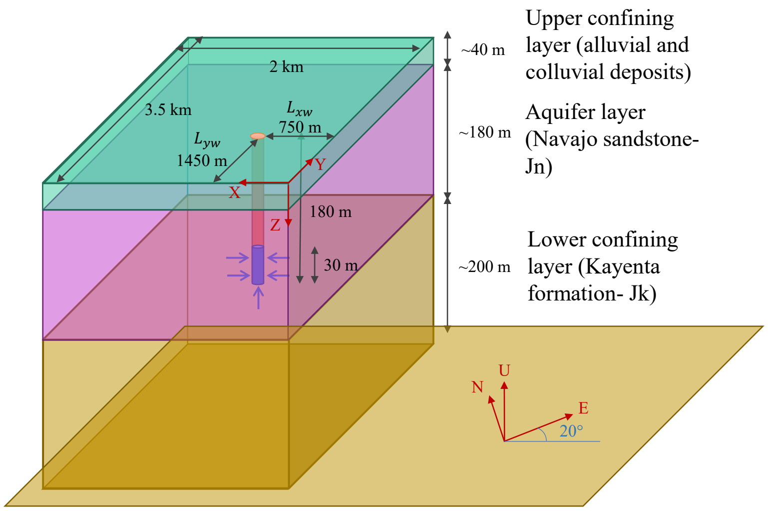

(a) Simplified conceptual model of the Anderson Junction aquifer system.

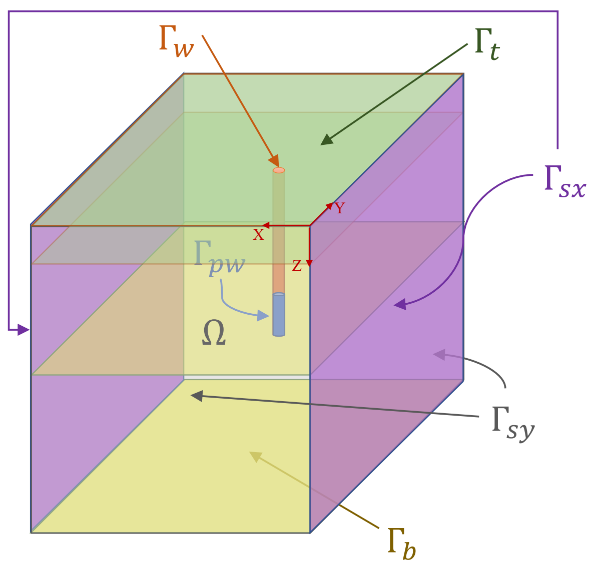

(b) Aquifer model illustrating the domain and defined boundaries.

Figure 6: (a). Simplified conceptual model of the Anderson Junction aquifer system showcasing the dimensions, names, formations, and thicknesses of the layers within the cross-section. The pumping well is accurately positioned and labeled in the 3D model. The figure also illustrates the model coordinate system in relation to the ENU global coordinate system. (b). Aquifer model illustrating the domain and defined boundaries referenced in the table 4, domain not to scale. Γ_b is the bottom boundary, Γ_t is the top boundary, Γ_{sx} is the two sides with normal facing in the X-direction, Γ_{sy} is two sides with normal facing in the Y-direction, Γ_w is the well boundary from the surface until the end of the casing set and Γ_{pw} is the screened area of the well boundary where water is pumped. Both domains are not to scale.

Description	Symbol	Unit	Value
Fluid source	f_p	s^{-1}	0.0
Body force	f_u	$N\,m^{-3}$	0.0
Specific weight of water	ρg	$N\,m^{-3}$	9807
Pumping rate	P_r	$m^3\,s^{-1}$	0.07
Pumping area	A	m^2	1473.4
Pumping time	T_p	d	4.0

Table 2: Model parameters

Description	Symbol	Unit	Upper conf.	Aquifer	Lower conf.
Porosity	ϕ	-	10%	32%	8%
Biot coefficient	α	-	0.868	0.998	0.858
Specific storage	S_ϵ	Pa^{-1}	0.8×10^{-10}	1.5×10^{-10}	0.8×10^{-10}
Shear modulus	μ_s	Pa	7.7×10^{9}	5.06×10^{9}	7.9×10^{9}
Lame's first param.	λ	Pa	6.088×10^{9}	3.768×10^{9}	6.156×10^{9}
Hydraulic conductivity xx	k_{xx}	$m^3\,s\,kg^{-1}$	5×10^{-12}	1.1×10^{-8}	5×10^{-12}
Hydraulic conductivity yy	k_{yy}	$m^3\,s\,kg^{-1}$	5×10^{-12}	4.7×10^{-10}	5×10^{-12}
Hydraulic conductivity zz	k_{zz}	$m^3\,s\,kg^{-1}$	5×10^{-12}	5×10^{-7}	5×10^{-12}

Table 3: Material parameters of the layers. The Anderson Junction site is an extensional tectonic regime, which usually leads to more vertical than horizontal faults, thereby increasing the value of k_{zz} over k_{xx} and k_{yy}.

The boundary conditions were established using USGS sources (Marston and Heilweil, 2012; Heilweil et al., 2000) and the parameters of the Biot equations for the aquifer layer were extracted from various regional studies (Torabi et al., 2015; Cheng and Toksöz, 1979; Loope et al., 2020) and sandstone properties studies (Batzle et al., 2007; George et al., 2010; Molina et al., 2017).

The estimate for aquifer hydraulic conductivity was derived from the permeability in Heilweil and Hsieh (2006) following

$$k = \frac{\kappa'}{\rho g}, \tag{4}$$

where k is the hydraulic conductivity, κ' is the specific permeability of the porous medium and ρg is the fluid's specific weight.

For the confining layer properties we employ porosity-based estimation (Dehghani et al., 2018). We used (Dehghani et al., 2018, Figure 5) for approximating the Biot coefficient, (Dehghani et al., 2018, Figure 7) for Biot's modulus, (Dehghani et al., 2018, Figure 8b) for Young's modulus and (Dehghani et al., 2018, Figure 9) for the shear modulus. We suppose the porosity of the upper confining layer to be 10 % following the suggestion of 7 % to 10 % in Qi et al. (2022) and Earle (2019). Considering the general trend of decreasing porosity and permeability with depth below the land surface (Herod, 2013), we assume the porosity of the lower confining layer to be 8 %. The average total porosity of the aquifer layer was derived from Heilweil et al. (2000).

5.2. Boundary conditions

Table 4 shows the boundary conditions for the state variables u (displacement), p (pressure) and q (flux). The boundaries referenced in the table are defined in fig. 6b.

During the aquifer test period, precipitation and evapotranspiration is assumed to be negligible compared with pumping, allowing us to assume no recharge through the top boundary Γ_t. We also assume no fluid flux on all other boundaries due to the presence of faults, except the pumping well boundary Γ_{pw}, where the extraction rate g_p is specified.

As the study area is not urban, the top boundary Γ_t is considered traction-free. We also assume there is no displacement on the bottom boundary Γ_b. We also assume zero normal displacement at the side boundaries Γ_{sx} and Γ_{sy} and well boundary Γ_w, and traction-free boundary conditions at the top surface Γ_t and at the pumping well boundary Γ_{pw}.

	Boundary condition	Boundary
Fluid problem (q, p)	$q \cdot n = 0$	$\Gamma_b \cup \Gamma_{sx} \cup \Gamma_{sy} \cup \Gamma_t \cup \Gamma_w$
	$q \cdot n = g_p = -P_r/A$	Γ_{pw}
Solid problem (u)	$u = 0$	Γ_b
	$u_x = 0$	Γ_{sx}
	$u_y = 0$	Γ_{sy}
	$\sigma \cdot n = 0$	$\Gamma_t \cup \Gamma_{pw}$
	$u \cdot n = 0$	Γ_w

Table 4: Boundary conditions of fluid and solid problem. The boundary sets are defined in fig. 6b.

5.3. Main modelling assumptions

We briefly discuss the main modelling assumptions and their justification. Our modelling approach is a parsimonious one, prioritising model simplicity over capturing all possible features of the real Anderson Junction site.

As in Burbey (2006), we assume a purely elastic deformation of the skeleton, i.e. no inelastic deformation. This is an acceptable assumption in the context of a single constant pumping cycle (as opposed to cyclic and/or pulsed pumping), however, this elasticity assumption may be invalid if we wanted to simulate subsidence across multiple seasons and using more complex pumping regimes.

We assume that seasonal recharge and evapotranspiration is zero; for this site this is a valid assumption if the pumping test occurs during the summer months due to the cold semi-arid (steppe) climate (BSk - Köppen type system).

The solid boundary condition on the capped well boundary Γ_{pw} is zero normal component of the deformation. The physicality of this boundary condition is discussed in Burbey (2006); in summary, it is likely that deformation near the well boundary are inaccurate due to localised effects such as sand grains near the well screen not being radially constrained during strong pumping. Consequently, the deformation and flux patterns given by the simulation in the region immediately around the well should be considered as indicative or approximate, rather than precise.

We do not model the fluid flow through fractures in our model explicitly,

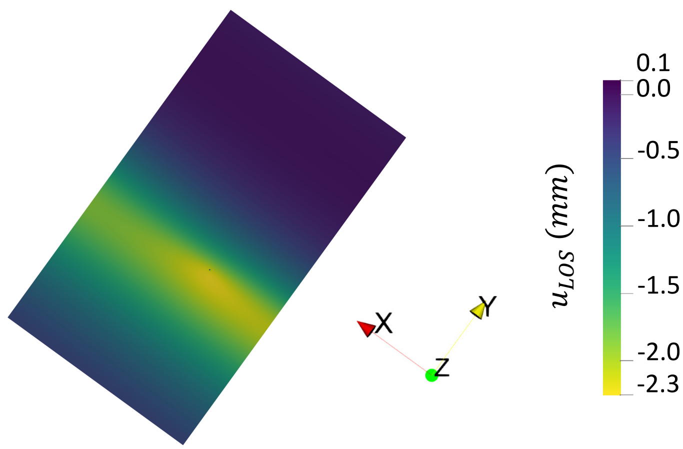

Figure 7: Simulated LOS surface displacement at the end of pumping for Anderson Junction test (4 d, P_r).

e.g. Berre et al. (2019), but instead incorporate their dominating effect on the fluid flow through the anisotropic hydraulic conductivity tensor. In the broader context of data assimilation, it is unlikely that SAR or GPS displacement data could be sufficiently informative to constrain information about microstructural features such as individual fracture paths. Further on this point of information content, we remark that Alghamdi (2020) demonstrated that SAR data is not informative about the variability of hydraulic conductivity in the vertical (z) direction. With this limited information content in mind, we also assume that the global anisotropic behaviour of the model is in the fluid problem, i.e. we treat the solid problem as isotropic. This is the same assumption used in Burbey (2006).

6. Results and discussion

6.1. Simulation of the Anderson Junction pumping test

Figure 7 shows the simulated LOS displacement after four days of pumping. The areas close to the pumping well exhibit LOS displacements on the order of 2.3 mm. The larger vertical displacements along the x direction (versus the y direction) are driven by the higher hydraulic conductivity in the x

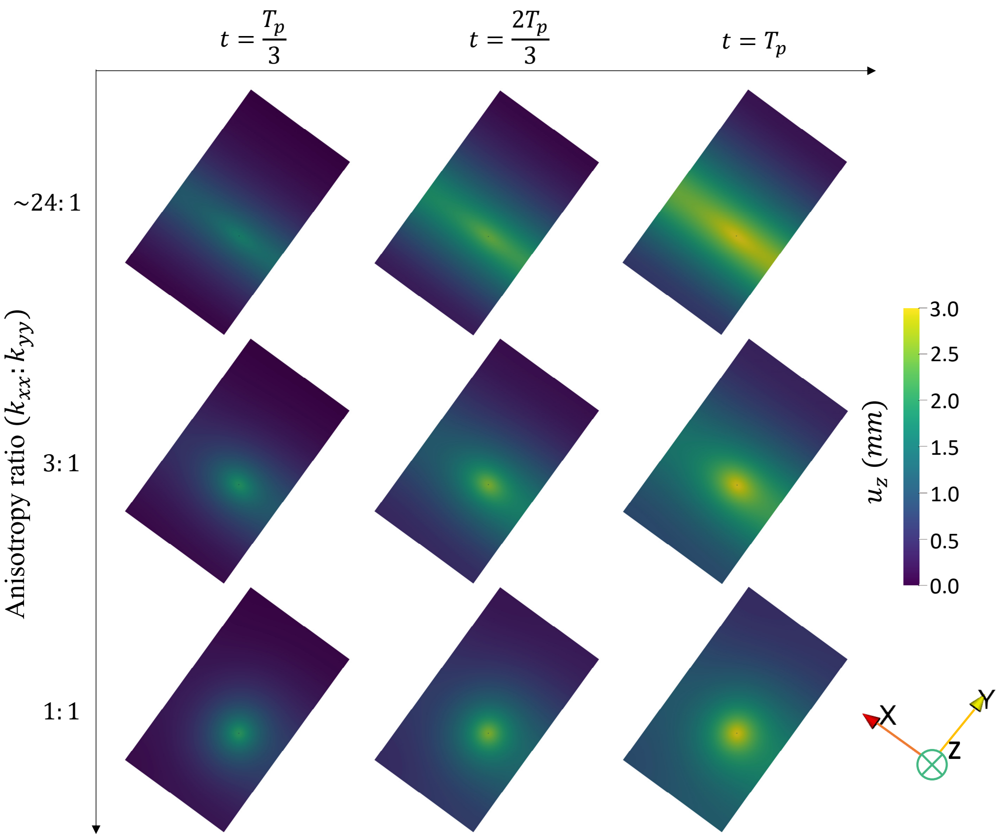

Figure 8: Surface displacements for three simulated scenarios: IHC, AHC with a 3:1 anisotropy ratio, and AHC with an anisotropy ratio of approximately 24:1. The images display the surface displacements at three times during the pumping phase.

direction.

6.2. The effect of anisotropy ratio on the surface displacement

We now conduct simulations with varying anisotropy ratios. Figure 8 presents the surface displacement for three simulated scenarios at three times through the pumping phase. The scenarios are IHC with $k_{xx} = k_{yy} = 0.6 \times k_{yy}^{AJ}$; AHC with a 3:1 anisotropy ratio, similar to the anisotropy observed in Burbey et al. (2006); Burbey (2006), where $k_{xx} = 3 \times 1.7 \times k_{yy}^{AJ}$ and $k_{yy} = 1.7 \times k_{yy}^{AJ}$; and AHC with an anisotropy ratio of about 24:1, representative of the Anderson Junction aquifer, where k_{xx}^{AJ} and k_{yy}^{AJ} are hydraulic conductivity in table 3. We selected the scaling values for k_{xx} and k_{yy} to achieve a similar range of displacements between the scenarios, making comparison easier. The hydraulic conductivity in the z direction remains constant across all scenarios.

These simulations show distinct patterns in surface displacement. The IHC scenario exhibits circular surface displacements. In contrast, the AHC simulations demonstrate elliptical surface displacement and the higher the anisotropy ratio the more pronounced the elliptical shape becomes.

6.3. Possibility of using InSAR to determine AHC in aquifers

We now aim to ascertain whether the surface displacement resulting from our model of the Anderson Junction aquifer pumping test can be detected using InSAR. We also explore the scenarios of higher pumping rates and/or a longer duration of pumping to understand if such a pumping test could lead to observable surface displacements with InSAR.

As explained in section 4, successful detection of surface displacement using Sentinel-1 InSAR requires displacements exceeding 8 mm along the LOS within a specific region around the well, e.g. an elliptical displacement pattern that demonstrates AHC. Figure 9 illustrates the surface displacement along line xx' and yy' at various time points. It is evident that the maximum surface displacement is only 3 mm. Consequently, under our conceptual model assumptions, the magnitude of the surface displacements created during the original Anderson Junction test described in Heilweil and Hsieh (2006) was likely insufficient to be detected by Sentinel-1 InSAR.

Despite this negative result, the model gives us a tool to explore under which scenarios a future test at Anderson Junction could produce a sufficient response detectable by InSAR and contain valuable information for inferring AHC. To this end, we explored three alternative scenarios. For reference in the following discussion, the LOS surface displacement under the original Anderson Junction test conditions is shown in fig. 7.

In the first scenario, *high pumping rate*, shown in fig. 10a we increase the pumping rate to eight times the value used in the original Anderson Junction test, while keeping the pumping duration fixed. The maximum line of sight displacement increased to 18 mm (detectable by InSAR), and the displacement pattern has a strong elliptical character.

In the second scenario, *long pumping duration*, shown in fig. 10b, we increase the pumping time to 32 d and keep the pumping rate the same as that used in the original Anderson Junction test. The maximum line of sight displacement is significantly lower than the first scenario at 8.6 mm,

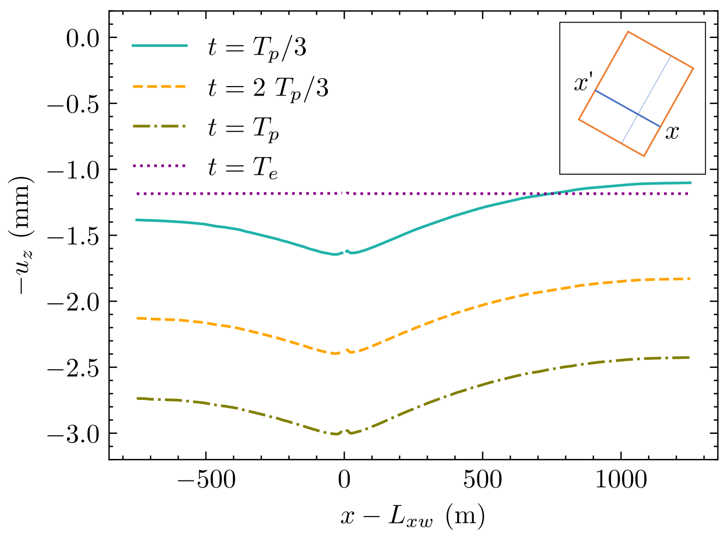

(a) Negative vertical surface displacement along xx'

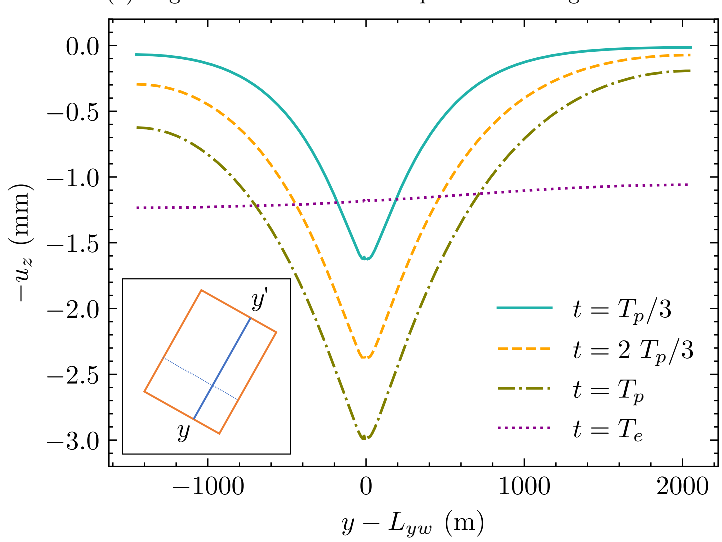

(b) Negative vertical surface displacement along yy'

Figure 9: Negative vertical surface displacement along line xx' and line yy' at different time points. The maximum predicted surface displacement during the pump test reaches 3 mm.

although still potentially at the threshold for detection by Sentinel-1 InSAR. Additionally, the longer pumping has led to a significantly more diffuse and isotropic displacement response than in the high pumping rate scenario. This can be attributed to the longer pumping having sufficient time to activate the slower diffusion timescale of the fluid problem along the minor axis Y.

Finally, we show an *intermediate rate and duration* scenario, shown in fig. 10c with eight days of pumping and four times the pumping rate of the original Anderson Junction test. This scenario is a compromise between the high pumping rate scenario fig. 10a and the long pumping rate scenario fig. 10b. We can see that a strong elliptical LOS displacement pattern is visible and that the maximum displacement at 13.3 mm exceeds the threshold for detection by Sentinel-1 InSAR. Note that by design the total water extracted

$$Q = \int_0^{T_p} \int_{\Gamma_{pw}} g_p \, \mathrm{d}x \, \mathrm{d}t, \tag{5}$$

is the same in the three scenarios.

Figure 11 presents a comparison of LOS surface displacement for the different scenarios along line xx' and yy'. Notably, the graph shows that along line yy', the high pumping rate causes substantial surface displacement gradients around the pumping well, which could result in sinking and fissure formation (Galloway et al., 1999, p. 132–133) (although, our model cannot predict this type of localized process directly).

We conclude that in terms of maximising the potential information content with respect to inferring possible anisotropy, it is important to strongly perturb the system via the pumping rate to ensure that the anisotropic character is visible *and* to pump a sufficient volume of water such that the LOS surface displacement can be detected by the chosen InSAR technology. However, it is important to note that there are practical limitations to how much we can increase the pumping rate or pumping duration, as they must align with the aquifer's properties, sustainability considerations and engineering considerations, see e.g. (Osborne, 1993) for a discussion.

6.4. The required aquifer test features for using SAR Data

In assessing the potential utility of SAR data for studying an aquifer system undergoing an aquifer test, several key considerations need to be taken into account, including the availability of data, the temporal resolution of SAR mission and accuracy of surface displacement measurements. The temporal resolution of the SAR data is important in case of acquiring more SAR

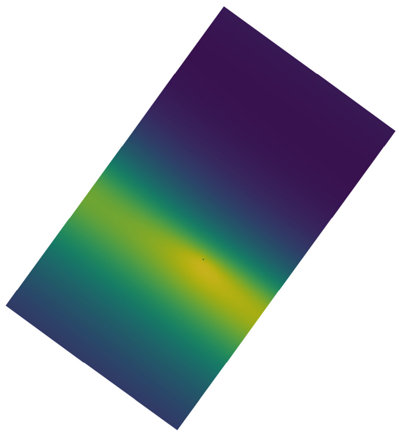

(a) High pumping rate
(4d, $8P_r$)
Max LOS def. = 18.0 mm

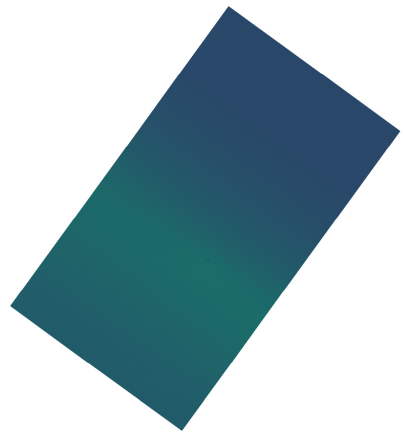

(b) Long pumping duration
(32d, P_r)
Max LOS def. = 8.6 mm

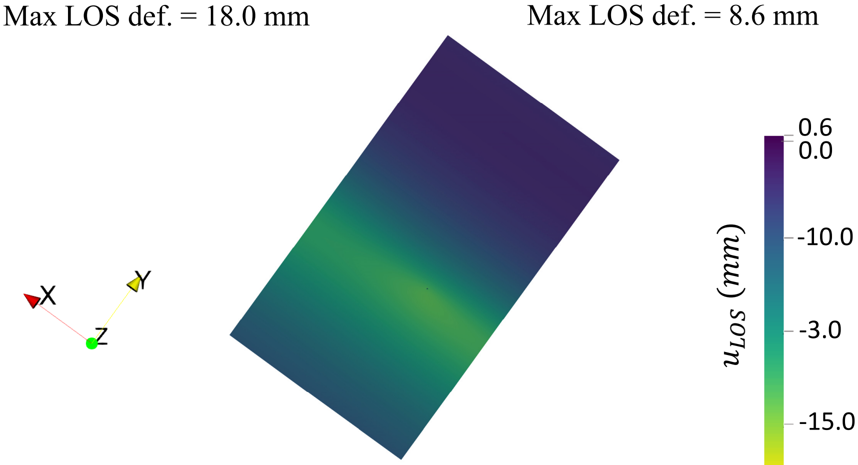

(c) Intermediate rate and duration
(8d, $4P_r$)
Max LOS def. = 13.3 mm

Figure 10: Simulated LOS surface displacement at the end of pumping for: (a) an 8 times pumping rate compared to the Anderson Junction test. (b) an extended pumping duration of 32 d, replicating the aquifer test characteristics of Anderson Junction (c) an extended intermediate pumping with 4 times rate and 8 d duration. In all cases, the total volume of extracted groundwater is the same. Note the different colorbar scale to fig. 7.

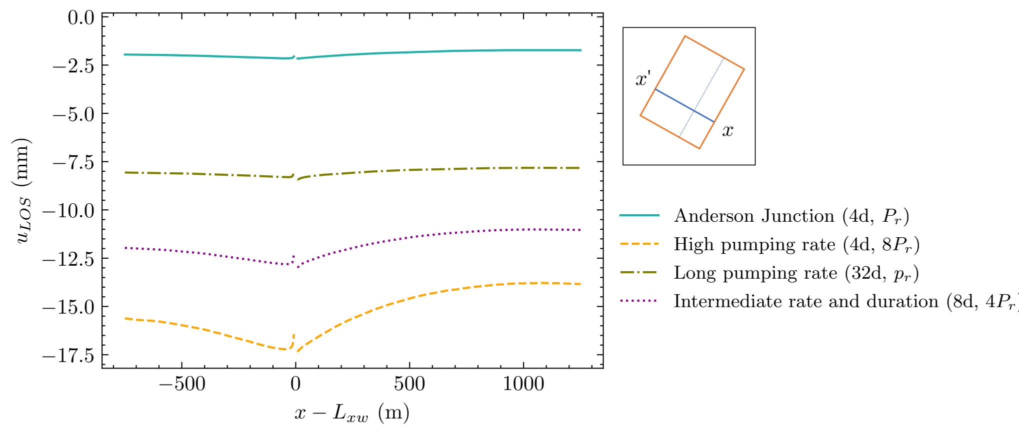

(a) LOS surface displacement along xx'

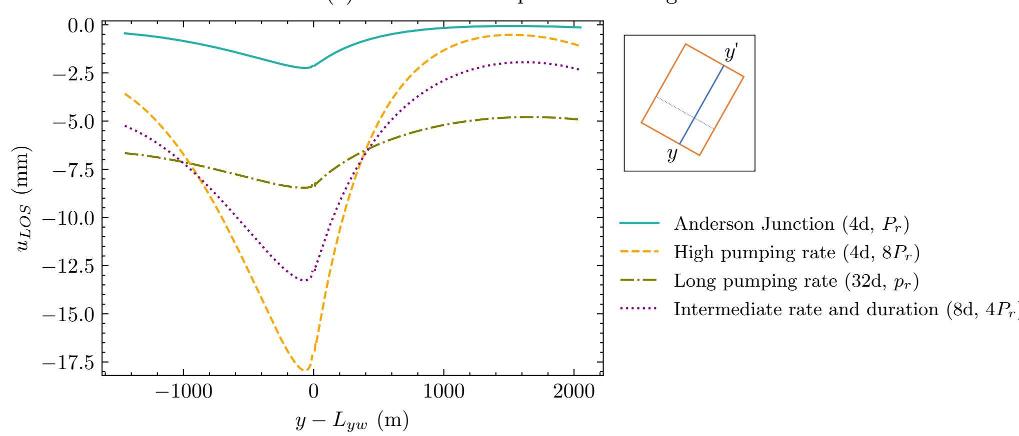

(b) LOS surface displacement along yy'

Figure 11: Comparison of LOS surface displacement along line xx' and line yy' at the end of pumping (T_p) for different pumping scenarios. Along yy', excessive pumping leads to significant surface displacement, which could lead to sinking and the formation of fissures near the pumping well (Galloway et al., 1999, p. 132–133).

data around the aquifer test time. We need at least one suitable pair of InSAR data within the aquifer test interval like in Alghamdi (2020) study, although having multiple data points within a longer test interval can enhance the understanding of the aquifer system. Moreover, it is crucial to assess whether the surface displacement caused by the aquifer test is observable through InSAR techniques. Therefore this is one of our motivations to build the proposed model to predict the surface displacement in the Anderson Junction aquifer.

In summary, to ensure the feasibility of using SAR data to estimate anisotropic aquifer properties, four key considerations should be taken into account when designing the aquifer test:

1. Availability of SAR data: It is essential to confirm the availability of SAR datasets specifically for the time and location of the aquifer test.

2. Adequate test interval: The aquifer test should have a sufficiently long time interval. This allows for the collection of multiple SAR data sets, enabling a more comprehensive study of the aquifer over time.

3. Sufficient total water extraction to ensure high LOS displacement: The observed LOS displacement should exceed a minimum threshold, e.g. 8 mm or more for the Sentinel-1 mission (Cigna et al., 2021).

4. A sufficiently high pumping rate to activate anisotropic behaviour: to ensure a elliptical displacement response driven by the activation of the flow on the major principal axis vs the minor principal axis.

7. Conclusions

We have developed an anisotropic poroelastic finite element model of the Anderson Junction site that is capable of predicting coupled fluid flow and displacements. Our results show that the effective elastic response of the aquifer at the Earth's surface has an anisotropic nature driven by the underlying anisotropy in the fluid problem, even when the elasticity problem is assumed to be isotropic. In the LOS displacement, this anisotropy manifests as distinctive elliptical patterns.

Under our model assumptions, the original Anderson Junction aquifer test described in (Heilweil and Hsieh, 2006) probably did not exhibit sufficient surface displacement for detection using InSAR. In three alternative scenarios, we explored longer pumping and/or higher pumping rates to explore the potential of using InSAR data to calibrate aquifer models with AHC – in two of these scenarios, see fig. 10a and fig. 10c, we predict LOS displacement levels necessary for detection by the contemporary Sentinel-1 InSAR mission. We add that the proposed model can be adapted to another aquifer test with a longer pumping and/or higher pumping rate or another confined aquifer system by changing the properties of the aquifer. It is also recommended to conduct extended pumping duration to gather InSAR data from multiple satellite passes.

Our upcoming research will explore two directions. First, due to uncertainty in the hydraulic conductivity tensor, we want to develop a stochastic model of AHC that respects the underlying material symmetries, e.g. (Cowin and Doty, 2007, Chapter 5). Second, with this stochastic model developed, we plan to assimilate InSAR-derived data into our aquifer model. This entails collecting field and remote sensing data to assess aquifer discharge and recharge dynamics. InSAR will offer valuable insights into surface displacement and underlying aquifer structures. By solving the inverse problem using spatiotemporal data, we aim to estimate aquifer properties following e.g. Alghamdi et al. (2020, 2021). These investigations promise to significantly advance our understanding of aquifers with AHC behavior leading to models with improved predictive power for use in a groundwater management context.

Acronyms

AHC anisotropic hydraulic conductivity. 1–5, 10, 19, 20, 26

FEM Finite Element Method. 37

GNSS Global Navigation Satellite System. 13

GPS Global Positioning System. 4

IHC isotropic hydraulic conductivity. 4, 19, 20

InSAR Interferometric Synthetic Aperture Radar. 1–5, 13, 20, 22, 25, 26

LOS Line of Sight. 5, 10, 13, 18, 20, 22–26

SAR Synthetic Aperture Radar. 10, 12, 22, 25

USGS US Geological Survey. 5

Acknowledgments

We would like to thank Natascha Kuhlmann from the University of Bonn for her assistance in interpreting the geologic maps and providing insights into the geological characteristics of the study area. We would also like to thank Hamid Dehghani from the Luxembourg Institute of Science and Technology (LIST) for his guidance selecting appropriate poroelastic constants.

Funding

This work was funded in whole, or in part, by the Luxembourg National Research Fund (FNR), grant reference PRIDE/17/12252781. For the purposes of open access, and in fulfilment of the obligations arising from the grant agreement, the authors have applied a Creative Commons Attribution 4.0 International (CC BY 4.0) license to any Author Accepted Manuscript version arising from this submission.

Authorship statement

Sona Salehian Ghamsari: Data curation, Methodology, Software, Formal analysis, Investigation, Writing - Original Draft, Validation, Visualization.
Tonie van Dam: Conceptualization, Writing - Review & Editing, Funding acquisition, Supervision.
Jack S. Hale: Conceptualization, Methodology, Software, Investigation, Writing - Review & Editing, Funding acquisition, Project administration, Supervision.

Supplementary material

The supplementary material (Salehian Ghamsari and Hale, 2024) includes code, input data and mathematical details of the finite element solver alongside a Docker container to execute the code in. We have also included a video version of fig. 7 showing the deformation of the Anderson Junction simulation.

Code availability section

AHC-Poroelastic-Model

Contact: salehiyan.sona@gmail.com.

Hardware requirements: x86-64 or ARM computer with container runtime e.g. Docker.

Program language: Python

Software required: Python, Paraview with Python interface (pvpython), Docker, DOLFINx.

The source code and Docker image are available for download at https://github.com/sonaselehian/ahc-poroelastic-model and at (Salehian Ghamsari and Hale, 2024).

References

Alghamdi, A., 2020. Bayesian inverse problems for quasi-static poroelasticity with application to ground water aquifer characterization from geodetic data. Thesis. University of Texas at Austin. doi:10.26153/tsw/13182.

Alghamdi, A., Hesse, M.A., Chen, J., Ghattas, O., 2020. Bayesian Poroelastic Aquifer Characterization From InSAR Surface Deformation Data. Part I: Maximum A Posteriori Estimate. Water Resources Research 56, e2020WR027391. doi:10.1029/2020WR027391.

Alghamdi, A., Hesse, M.A., Chen, J., Villa, U., Ghattas, O., 2021. Bayesian Poroelastic Aquifer Characterization From InSAR Surface Deformation Data. 2. Quantifying the Uncertainty. Water Resources Research 57, e2021WR029775. doi:10.1029/2021WR029775.

Amitrano, D., Martino, G.D., Iodice, A., Mitidieri, F., Papa, M.N., Riccio, D., Ruello, G., 2014. Sentinel-1 for monitoring reservoirs: A performance analysis. Remote Sensing 6, 10676–10693. doi:10.3390/rs61110676.

Baratta, I.A., Dean, J.P., Dokken, J.S., Habera, M., Hale, J.S., Richardson, C.N., Rognes, M.E., Scroggs, M.W., Sime, N., Wells., G.N., 2023. Dolfinx: The next generation fenics problem solving environment. Zenodo doi:10.5281/zenodo.10447666.

Basu, N.B., Van Meter, K., 2014. 4.3 - Sustainability of Groundwater Resources, in: Ahuja, S. (Ed.), Comprehensive Water Quality and Purification. Elsevier, Waltham, pp. 57–75. doi:10.1016/B978-0-12-382182-9.00062-1.

Batzle, M., Duranti, L., Rector, J., Pride, S., 2007. Measurment and Interpretation of Seismic Attenuation for Hydrocarbon Exploration. Technical Report. Colorado School of Mines, Golden, CO (United States). doi:10.2172/927592.

Berre, I., Doster, F., Keilegavlen, E., 2019. Flow in Fractured Porous Media: A Review of Conceptual Models and Discretization Approaches. Transport in Porous Media 130, 215–236. doi:10.1007/s11242-018-1171-6.

Biot, M.A., 1941. General Theory of Three-Dimensional Consolidation. Journal of Applied Physics 12, 155–164. doi:10.1063/1.1712886.

Bonì, R., Cigna, F., Bricker, S., Meisina, C., McCormack, H., 2016. Characterisation of hydraulic head changes and aquifer properties in the London Basin using Persistent Scatterer Interferometry ground motion data. Journal of Hydrology 540, 835–849. doi:10.1016/j.jhydrol.2016.06.068.

Bonì, R., Meisina, C., Cigna, F., Herrera, G., Notti, D., Bricker, S., McCormack, H., Tomás, R., Béjar-Pizarro, M., Mulas, J., Ezquerro, P., 2017. Exploitation of Satellite A-DInSAR Time Series for Detection, Characterization and Modelling of Land Subsidence. Geosciences 7. doi:10.3390/geosciences7020025.

Brenner, S.C., Scott, L.R., 2008. The Mathematical Theory of Finite Element Methods. volume 15 of *Texts in Applied Mathematics*. Springer, New York, NY. doi:10.1007/978-0-387-75934-0.

Brezzi, F., Douglas, J., Marini, L.D., 1985. Two families of mixed finite elements for second order elliptic problems. Numerische Mathematik 47, 217–235. doi:10.1007/BF01389710.

Burbey, T.J., 2006. Three-dimensional deformation and strain induced by municipal pumping, part 2: Numerical analysis. Journal of Hydrology 330, 422–434. doi:10.1016/j.jhydrol.2006.03.035.

Burbey, T.J., Warner, S.M., Blewitt, G., Bell, J.W., Hill, E., 2006. Three-dimensional deformation and strain induced by municipal pumping, part 1: Analysis of field data. Journal of Hydrology 319, 123–142. doi:10.1016/j.jhydrol.2005.06.028.

Caretta, M., Mukherji, A., Arfanuzzaman, M., Betts, R., Gelfan, A., Hirabayashi, Y., Lissner, T., Liu, J., Gunn, E.L., Morgan, R., Mwanga, S., Supratid, S., 2022. Water. In: Climate Change 2022: Impacts, Adaptation and Vulnerability. Technical Report. Cambridge University Press, Cambridge, UK and New York, NY, USA. doi:10.1017/9781009325844.006.

Chaussard, E., Bürgmann, R., Shirzaei, M., Fielding, E.J., Baker, B., 2014. Predictability of hydraulic head changes and characterization of aquifer-system and fault properties from InSAR-derived ground deformation. Journal of Geophysical Research: Solid Earth 119, 6572–6590. doi:10.1002/2014JB011266.

Cheng, C.H., Toksöz, M.N., 1979. Inversion of seismic velocities for the pore aspect ratio spectrum of a rock. Journal of Geophysical Research: Solid Earth 84, 7533–7543. doi:10.1029/JB084iB13p07533.

Chouly, F., Hild, P., Renard, Y., 2015. Symmetric and non-symmetric variants of Nitsche's method for contact problems in elasticity: theory and numerical experiments. Mathematics of Computation 84, 1089–1112. doi:10.1090/S0025-5718-2014-02913-X.

Cigna, F., Esquivel Ramírez, R., Tapete, D., 2021. Accuracy of Sentinel-1 PSI and SBAS InSAR Displacement Velocities against GNSS and Geodetic Leveling Monitoring Data. Remote Sensing 13. doi:10.3390/rs13234800.

Cowin, S.C., Doty, S.B., 2007. Tissue mechanics. Springer. doi:10.1007/978-0-387-49985-7.

Dehghani, H., Penta, R., Merodio, J., 2018. The role of porosity and solid matrix compressibility on the mechanical behavior of poroelastic tissues. Materials Research Express 6, 035404. doi:10.1088/2053-1591/aaf5b9.

Duan, W., Zhang, H., Wang, C., Tang, Y., 2020. Multi-temporal insar parallel processing for sentinel-1 large-scale surface deformation mapping. Remote Sensing 12. doi:10.3390/rs12223749.

Earle, S., 2019. 14.1 Groundwater and Aquifers URL: https://opentextbc.ca/physicalgeology2ed/chapter/14-1-groundwater-and-aquifers/.

Erkens, G., Bucx, T., Dam, R., de Lange, G., Lambert, J., 2015. Sinking coastal cities. Proceedings of the International Association of Hydrological Sciences 372, 189–198. doi:10.5194/piahs-372-189-2015.

European Space Agency (ESA), 2023. User Guides - Sentinel-1 SAR - Interferometric Wide Swath - Sentinel Online. URL: https://sentinels.copernicus.eu/web/sentinel/user-guides.

Famiglietti, J.S., Lo, M., Ho, S.L., Bethune, J., Anderson, K.J., Syed, T.H., Swenson, S.C., de Linage, C.R., Rodell, M., 2011. Satellites measure recent rates of groundwater depletion in California's Central Valley. Geophysical Research Letters 38. doi:10.1029/2010GL046442.

Ferronato, M., Castelletto, N., Gambolati, G., 2010. A fully coupled 3-D mixed finite element model of Biot consolidation. Journal of Computational Physics 229, 4813–4830. doi:10.1016/j.jcp.2010.03.018.

Food and Agriculture Organization of the United Nations (FAO), 2022. Water. URL: http://www.fao.org/water/en/.

Fuhrmann, T., Garthwaite, M.C., 2019. Resolving Three-Dimensional Surface Motion with InSAR: Constraints from Multi-Geometry Data Fusion. Remote Sensing 11, 241. doi:10.3390/rs11030241.

Galloway, D.L., Burbey, T.J., 2011. Review: Regional land subsidence accompanying groundwater extraction. Hydrogeology Journal 19, 1459–1486. doi:10.1007/s10040-011-0775-5.

Galloway, D.L., Hoffmann, J., 2007. The application of satellite differential SAR interferometry-derived ground displacements in hydrogeology. Hydrogeology Journal 15, 133–154. doi:10.1007/s10040-006-0121-5.

Galloway, D.L., Jones, D.R., Ingebritsen, S.E., 1999. Land subsidence in the United States. volume 1182. Geological Survey (USGS). doi:10.3133/cir1182.

Gambolati, G., Teatini, P., 2015. Geomechanics of subsurface water withdrawal and injection. Water Resources Research 51, 3922–3955. doi:10.1002/2014WR016841.

George, N., Akpan, A., George, A., Obot, I., 2010. Determination of elastic properties of the overburden materials in parts of Akamkpa, southeastern Nigeria using seismic refraction studies. Archives of Physics Research 1, 58–71. ISSN: 0976-0970.

Geuzaine, C., Remacle, J.F., 2009. Gmsh: A 3-D finite element mesh generator with built-in pre- and post-processing facilities. International Journal for Numerical Methods in Engineering 79, 1309–1331. doi:10.1002/nme.2579.

Guo, L., Gong, H., Zhu, F., Zhu, L., Zhang, Z., Zhou, C., Gao, M., Sun, Y., 2019a. Analysis of the spatiotemporal variation in land subsidence on the Beijing Plain, china. Remote Sensing 11. doi:10.3390/rs11101170.

Guo, Q., Huang, J., Zhou, Z., Wang, J., 2019b. Experiment and Numerical Simulation of Seawater Intrusion under the Influences of Tidal Fluctuation and Groundwater Exploitation in Coastal Multilayered Aquifers. Geofluids doi:10.1155/2019/2316271.

Guzy, A., Malinowska, A.A., 2020. State of the art and recent advancements in the modelling of land subsidence induced by groundwater withdrawal. Water 12. doi:10.3390/w12072051.

Haagenson, R., Rajaram, H., Allen, J., 2020. A generalized poroelastic model using fenics with insights into the noordbergum effect. Computers & Geosciences 135, 104399. doi:10.1016/j.cageo.2019.104399.

Haghighi, M.H., Motagh, M., 2019. Ground surface response to continuous compaction of aquifer system in Tehran, Iran: Results from a long-term multi-sensor InSAR analysis. Remote Sensing of Environment 221, 534–550. doi:10.1016/j.rse.2018.11.003.

Harbaugh, A.W., 2005. MODFLOW-2005 : the U.S. Geological Survey modular ground-water model–the ground-water flow process. Report 6-A16. doi:10.3133/tm6A16.

Harbaugh, A.W., Banta, E.R., Hill, M.C., McDonald, M.G., 2000. MODFLOW-2000, The U.S. Geological Survey modular ground-water model: User guide to modularization concepts and the ground-water flow process. Report 00-92. doi:10.3133/ofr200092.

Heilweil, V., Freethey, G.W., Wilkowske, C., Stolp, B.J., Wilberg, D.E., 2000. Geohydrology and numerical simulation of groundwater flow in the central Virgin River Basin of Iron and Washington Counties, Utah. Other Government Series 116. Utah Department of Natural Resources, Division of Water Rights. Salt Lake City, UT. URL: http://pubs.er.usgs.gov/publication/70179116.

Heilweil, V.M., Hsieh, P.A., 2006. Determining Anisotropic Transmissivity Using a Simplified Papadopulos Method. Groundwater 44, 749–753. doi:10.1111/j.1745-6584.2006.00210.x.

Helm, D., 1986. Compac: a field-tested model to simulate and predict subsidence due to fluid withdrawal. Austral Geomechan Comput Newslett 10, 18–20. URL: http://hdl.handle.net/102.100.100/272626?index=1.

Herod, M., 2013. Reading: Porosity and Permeability | Geology. URL: https://courses.lumenlearning.com/geo/chapter/reading-porosity-and-permeability/.

Herrera-García, G., Ezquerro, P., Tomás, R., Béjar-Pizarro, M., López-Vinielles, J., Rossi, M., Mateos, R.M., Carreón-Freyre, D., Lambert, J., Teatini, P., Cabral-Cano, E., Erkens, G., Galloway, D., Hung, W.C., Kakar, N., Sneed, M., Tosi, L., Wang, H., Ye, S., 2021. Mapping the global threat of land subsidence. Science 371, 34–36. doi:10.1126/science.abb8549.

Hesse, M.A., Stadler, G., 2014. Joint inversion in coupled quasi-static poroelasticity. Journal of Geophysical Research: Solid Earth 119, 1425–1445. doi:10.1002/2013JB010272.

Hintze, L., 1980. Geologic map of Utah: Utah Geological and Mineral Survey. URL: https://mrdata.usgs.gov/geology/state/map-us.html.

Hoffmann, J., Leake, S.A., Galloway, D.L., Wilson, A.M., 2003. MODFLOW-2000 ground-water model-user guide to the Subsidence and Aquifer-System Compaction (SUB) Package. Technical Report 2003-233. U.S. Geological Survey. doi:10.3133/ofr03233.

Hsieh, P.A., 1996. Deformation-Induced Changes in Hydraulic Head During Ground-Water Withdrawal. Groundwater 34, 1082–1089. doi:10.1111/j.1745-6584.1996.tb02174.x.

Hu, X., Bürgmann, R., 2020. Aquifer deformation and active faulting in Salt Lake Valley, Utah, USA. Earth and Planetary Science Letters 547, 116471. doi:10.1016/j.epsl.2020.116471.

Hu, X., Lu, Z., Wang, T., 2018. Characterization of Hydrogeological Properties in Salt Lake Valley, Utah, using InSAR. Journal of Geophysical Research: Earth Surface 123, 1257–1271. doi:10.1029/2017JF004497.

Hurlow, H.A., 1998. The geology of the central Virgin River Basin, southwestern Utah, and its relation to ground-water conditions. Number 26 in Water-resources bulletin / Utah Geological Survey, Utah Geological Survey, Utah Dept. of Natural Resources, Salt Lake City, UT. ISBN: 978-1-55791-614-3.

Langtangen, H.P., Logg, A., 2016. Solving PDEs in Python. Springer International Publishing. doi:10.1007/978-3-319-52462-7.

Li, S., Xu, W., Li, Z., 2022. Review of the SBAS InSAR Time-series algorithms, applications, and challenges. Geodesy and Geodynamics 13, 114–126. doi:10.1016/j.geog.2021.09.007.

Loope, D.B., Loope, G.R., Burberry, C.M., Rowe, C.M., Bryant, G.C., 2020. Surficial fractures in the Navajo sandstone, south-western USA: the roles of thermal cycles, rainstorms, granular disintegration, and iterative cracking. Earth Surface Processes and Landforms 45, 2063–2077. doi:10.1002/esp.4866.

Manunta, M., De Luca, C., Zinno, I., Casu, F., Manzo, M., Bonano, M., Fusco, A., Pepe, A., Onorato, G., Berardino, P., De Martino, P., Lanari, R., 2019. The parallel sbas approach for sentinel-1 interferometric wide swath deformation time-series generation: Algorithm description and products quality assessment. IEEE Transactions on Geoscience and Remote Sensing 57, 6259–6281. doi:10.1109/TGRS.2019.2904912.

Marston, T.M., Heilweil, V.M., 2012. Numerical simulation of groundwater movement and managed aquifer recharge from Sand Hollow Reservoir, Hurricane Bench area, Washington County, Utah. USGS Numbered Series 2012-5236. U.S. Geological Survey. Reston, VA. doi:10.3133/sir20125236.

Molina, O., Vilarrasa, V., Zeidouni, M., 2017. Geologic Carbon Storage for Shale Gas Recovery. Energy Procedia 114, 5748–5760. doi:10.1016/j.egypro.2017.03.1713.

Osborne, P.S., 1993. Suggested operating procedures for aquifer pumping tests. Ground water issue (15th in series). Technical Report. Environmental Protection Agency, Ada, Oklahoma (United States). Robert S. Kerr Environmental Research Laboratory Ada, Oklahoma. URL: https://www.epa.gov/remedytech.

Papadopulos, I.S., 1965. Nonsteady flow to a well in an infinite anisotropic aquifer, in: Proceedings of the Symposium on Hydrology of Fractured Rocks. URL: https://unesdoc.unesco.org/ark:/48223/pf0000141973.

Poland, J.F., 1984. Guidebook to studies of land subsidence due to groundwater withdrawal. URL: https://unesdoc.unesco.org/ark:/48223/pf0000065167.

Qi, Y., Ju, Y., Yu, K., Meng, S., Qiao, P., 2022. The effect of grain size, porosity and mineralogy on the compressive strength of tight sandstones: A case study from the eastern Ordos Basin, China. Journal of Petroleum Science and Engineering 208, 109461. doi:10.1016/j.petrol.2021.109461.

Salehian Ghamsari, S., Hale, J.S., 2024. Supplementary material for "Can the anisotropic hydraulic conductivity of an aquifer be determined using surface displacement data? A case study". doi:10.5281/zenodo.10890121.

Singh, A., 2014. Groundwater resources management through the applications of simulation modeling: A review. Science of The Total Environment 499, 414–423. doi:10.1016/j.scitotenv.2014.05.048.

Torabi, A., Gabrielsen, R., Fossen, H., Ringrose, P., Skurtveit, E., Andò, E., Marinelli, F., Viggiani, G., Dal Pont, S., Braathen, A., Hovland, A., Bésuelle, P., Alikarami, R., Zalmstra, H., Sokoutis, D., 2015. Strain localization in sandstone and its implications for CO2 storage. First Break 33, 81–92. doi:10.3997/1365-2397.33.7.81788.

U.S. Geological Survey, 2016. National Water Information System data available on the World Wide Web (USGS Water Data for the Nation). URL: http://waterdata.usgs.gov/nwis/. Accessed 31-05-2023.

Verruijt, A., 1969. Elastic Storage of Aquifers, in: Flow through Porous Media. Academic Press, New York, NY, USA, pp. 331–376.

Walker, G., Wang, Q.J., Horne, A.C., Evans, R., Richardson, S., 2020. Estimating groundwater-river connectivity factor for quantifying changes in irrigation return flows in the Murray–Darling Basin. Australasian Journal of Water Resources 24, 121–138. doi:10.1080/13241583.2020.1787702.

Zhou, C., Gong, H., Zhang, Y., Warner, T.A., Wang, C., 2018. Spatiotemporal Evolution of Land Subsidence in the Beijing Plain 2003–2015 Using Persistent Scatterer Interferometry (PSI) with Multi-Source SAR Data. Remote Sensing 10. doi:10.3390/rs10040552.

Appendix A. Finite element discretisation of Biot's poroelasticity model

In this appendix, we recall the three-field Finite Element Method (FEM) discretisation of Biot's theory which broadly follows the original development in Ferronato et al. (2010).

Appendix A.1. Notation

We recall the aquifer problem domain $\Omega \subset \mathbb{R}^3$ and its boundary Γ with outwards pointing normal n. For any subset ω of $\bar{\Omega} := \Omega \cup \Gamma$ we denote $L^2(\omega)$ as the usual Sobolev space of square integrable functions on ω, and $(\cdot, \cdot)_\omega$ the associated inner product, which for two arguments $f, g \in L^2(\omega)$ can be written

$$(f, g)_{L^2(\omega)} = \int_\omega fg \, \mathrm{d}x. \tag{A.1}$$

For brevity, we introduce the compact notation $(\cdot, \cdot)_\omega := (\cdot, \cdot)_{L^2(\omega)}$ and $(\cdot, \cdot) := (\cdot, \cdot)_{L^2(\Omega)}$. We can similarly denote $H^1(\omega)$ as the usual Sobolev space of square integrable functions with weak derivatives in $L^2(\omega)$ with associated inner product $(\cdot, \cdot)_{H^1(\omega)}$ defined as

$$(f, g)_{H^1(\omega)} = \int_\omega fg + \nabla f \nabla g \, \mathrm{d}x, \tag{A.2}$$

where ∇ is the usual gradient of a scalar function.

Finally, we introduce the slightly less standard Sobolev space $H(\mathrm{div}; \omega)$ as the space of Sobolev space of vector-valued square integrable functions with square integrable divergence on ω

$$H(\mathrm{div}; \Omega) = \{f : f \in (L^2(\Omega))^3 \ , \ \mathrm{div}\, f \in L^2(\Omega)\}, \tag{A.3}$$

where the div operator is acting on a vector-valued function f with components (f_1, f_2, f_3) can be written as

$$\mathrm{div}\, f := \nabla \cdot f := \frac{\partial f_1}{\partial x_1} + \frac{\partial f_2}{\partial x_2} + \frac{\partial f_3}{\partial x_3}. \tag{A.4}$$

Appendix A.2. Weak formulation

We briefly recall the strong form of the three-field formulation of Biot's equations that was outlined in section 3.1. Given a domain $\Omega \subset \mathbb{R}^3$ with boundary Γ find the fluid-pore pressure $p : \Omega \times (0,T] \to \mathbb{R}$, deformation $u : \Omega \times (0,T] \to \mathbb{R}^3$ and fluid flux $q : \Omega \times (0,T] \to \mathbb{R}^3$ such that

$$(S_\epsilon p + \alpha \nabla \cdot u)_t + \nabla \cdot q = f_p \text{ in } \Omega \times (0,T], \tag{A.5a}$$
$$-\nabla \cdot \bar{\sigma} = f_u \text{ in } \Omega \times (0,T], \tag{A.5b}$$
$$q + k\nabla p = 0 \text{ in } \Omega \times (0,T], \tag{A.5c}$$

with boundary conditions

$$u = u_d \text{ on } \Gamma_u^d \times (0,T], \tag{A.5d}$$
$$\bar{\sigma} \cdot n = g_u \text{ on } \Gamma_u^n \times (0,T], \tag{A.5e}$$
$$p = p_d \text{ on } \Gamma_p^d \times (0,T], \tag{A.5f}$$
$$q \cdot n = g_p \text{ on } \Gamma_p^n \times (0,T], \tag{A.5g}$$

where the boundary Γ has been partitioned into disjoint parts for both the solid problem $\Gamma = \Gamma_u^d \cup \Gamma_p^n$ and the fluid problem $\Gamma = \Gamma_p^d \cup \Gamma_p^n$ and initial conditions

$$p(x,0) = p^0 \text{ on } \Omega, \tag{A.5h}$$
$$u(x,0) = u^0 \text{ on } \Omega, \tag{A.5i}$$
$$q(x,0) = q^0 \text{ on } \Omega, \tag{A.5j}$$

To simplify what follows, but without loss of generality, we make the following regularity assumptions in space for the pressure

$$\mathcal{P} = \{p : \Omega \times [0,T] \to \mathbb{R} \mid p \in L^2(\Omega)\}, \tag{A.6a}$$
$$\mathcal{U} = \{u : \Omega \times [0,T] \to \mathbb{R}^3 \mid u \in (H^1(\Omega))^3,\ u = u_d \text{ on } \Gamma_u^d\}, \tag{A.6b}$$
$$\mathcal{Q} = \{q : \Omega \times [0,T] \to \mathbb{R}^3 \mid q \in H(\text{div};\Omega),\ q \cdot n = g_p \text{ on } \Gamma_p^n\}. \tag{A.6c}$$

Additional sufficient regularity assumptions in time are also required, which we ignore for simplicity.

To derive the weak form of the system eq. (A.5), we multiply eqs. (A.5a) to (A.5c) by test functions $\tilde{p} \in \mathcal{P}$, $\tilde{u} \in \mathcal{U}_0$, and $\tilde{q} \in \mathcal{Q}_0$, respectively, where

$$\mathcal{U}_0 = \{u \in \mathcal{U} \mid u_d = 0\}, \tag{A.7a}$$
$$\mathcal{Q}_0 = \{q \in \mathcal{Q} \mid g = 0\}, \tag{A.7b}$$

and then integrate over the domain Ω before applying any necessary integration by parts results.

Starting this process with eq. (A.5a) we straightforwardly obtain

$$((S_\epsilon p + \alpha \nabla \cdot u)_t, \tilde{p})_\Omega + (\nabla \cdot q, \tilde{p})_\Omega = (f_p, \tilde{p})_\Omega, \quad \forall \tilde{p} \in \mathcal{P}. \tag{A.8}$$

Continuing with eq. (A.5b), we obtain

$$(-\nabla \cdot \bar{\sigma}, \tilde{u})_\Omega = (f, \tilde{u})_\Omega \quad \forall \tilde{u} \in \mathcal{U}_0, \tag{A.9}$$

and then using integration by parts gives for all $\tilde{u} \in \mathcal{U}_0$

$$(\nabla \cdot \bar{\sigma}, \tilde{u})_\Omega = -(\bar{\sigma}, \nabla \tilde{u})_\Omega + (\bar{\sigma} n, \tilde{u})_\Gamma \quad \forall \tilde{u} \in \mathcal{U}_0. \tag{A.10}$$

Splitting the integral on the boundary into its two constituent parts

$$(\bar{\sigma} n, \tilde{u})_\Gamma = (\bar{\sigma} n, \tilde{u})_{\Gamma_u^d} + (\bar{\sigma} n, \tilde{u})_{\Gamma_u^n}, \tag{A.11}$$

and, using the definition of the space $\mathcal{U}_0$ and the knowledge that $\bar{\sigma} n = g_u$ on Γ_u^n, allows us to write

$$(\bar{\sigma}, \nabla \tilde{u})_\Omega = (f, \tilde{u})_\Omega + (g_u, \tilde{u})_{\Gamma_u^n}, \quad \forall \tilde{u} \in \mathcal{U}_0. \tag{A.12}$$

Finally, for equation eq. (A.5c) we obtain

$$(\nabla p, \tilde{q})_\Omega = -(k^{-1} q, \tilde{q})_\Omega, \quad \forall \tilde{q} \in \mathcal{Q}_0, \tag{A.13}$$

where k^{-1} denotes the inverse of k, and applying integration by parts on the term on the left hand side of eq. (A.13) gives

$$-(\nabla \cdot \tilde{q}, p)_\Omega + (p, \tilde{q} \cdot n)_\Gamma = -(k^{-1} q, \tilde{q}), \quad \forall \tilde{q} \in \mathcal{Q}_0. \tag{A.14}$$

Splitting the integral on the boundary into its two constituent parts

$$(p, \tilde{q} \cdot n)_\Gamma = (p, \tilde{q} \cdot n)_{\Gamma_p^d} + (p, \tilde{q} \cdot n)_{\Gamma_p^n}, \tag{A.15}$$

and using the definition of the space $\mathcal{Q}_0$ and the knowledge that $q \cdot n = g$ on Γ_p^n

$$-(k^{-1} q, \tilde{q})_\Omega + (p, \nabla \cdot \tilde{q})_\Omega = (p_d, \tilde{q} \cdot n)_{\Gamma_p^d}, \quad \forall \tilde{q} \in \mathcal{Q}_0. \tag{A.16}$$

In summary, the final variational problem is to find $p \in \mathcal{P}$, $u \in \mathcal{U}$, and $q \in \mathcal{Q}$ that satisfy the equations

$$((S_\epsilon p + \alpha \nabla \cdot u)_t, \tilde{p})_\Omega + (\nabla \cdot q, \tilde{p})_\Omega = (f_p, \tilde{p})_\Omega, \tag{A.17a}$$
$$(\bar{\sigma}(u, p), \nabla \tilde{u})_\Omega = (f, \tilde{u})_\Omega + (g_u, \tilde{u})_{\Gamma_u^n}, \tag{A.17b}$$
$$-(k^{-1} q, \tilde{q})_\Omega + (p, \nabla \cdot \tilde{q})_\Omega = (p_d, \tilde{q} \cdot n)_{\Gamma_p^d}. \tag{A.17c}$$

for all test functions $\tilde{p} \in \mathcal{P}$, $\tilde{u} \in \mathcal{U}_0$, and $\tilde{q} \in \mathcal{Q}_0$. We emphasise that in this three-field formulation the flux boundary condition eq. (A.5g) is built strongly into the space $\mathcal{Q}$ and the pressure boundary condition eq. (A.5f) occurs weakly in eq. (A.17c). By contrast, in the classical two-field formulation the flux boundary condition occurs weakly and the pressure boundary condition is built strongly into a space $\mathcal{P}$ with stronger H^1-regularity requirements.

Appendix A.3. Discretization in time

For discretizing eq. (A.17) in time, we use a first-order backwards Euler method, see e.g. Langtangen and Logg (2016) for full details.

Consider $M + 1$ time steps $0 = t^0 < t^1 < t^2 < \ldots < t^M = T$ uniformly spaced on the interval $[0, T]$ giving a constant timestep $\Delta t = \Delta t^n = t^{n+1} - t^n$ for $n \in 0, \ldots, M - 1$. The first-order backwards Euler scheme approximates the time derivative on the displacement u and pressure p as

$$(p^{n+1})_t \approx \frac{p^{n+1} - p^n}{\Delta t}, \quad \forall n \in 0, \ldots, M - 1, \tag{A.18a}$$
$$(u^{n+1})_t \approx \frac{u^{n+1} - u^n}{\Delta t}, \quad \forall n \in 0, \ldots, M - 1. \tag{A.18b}$$

Following standard arguments, and after some minor rearrangements, the discrete time version of eq. (A.17) can be written: For $n = 0, \ldots, M - 1$ find $p^{n+1} \in \mathcal{P}$, $u^{n+1} \in \mathcal{U}$, and $q^{n+1} \in \mathcal{Q}$ such that

$$(S_\epsilon p^{n+1} + \alpha \nabla \cdot u^{n+1} + \Delta t \nabla \cdot q^{n+1}, \tilde{p}) = (\Delta t f_p^{n+1} + S_\epsilon p^n + \alpha \nabla \cdot u^n, \tilde{p}), \tag{A.19a}$$
$$-(\bar{\sigma}(u^{n+1}, p^{n+1}), \nabla \tilde{u}) = -(f_u^{n+1}, \tilde{u}) - (g_u^{n+1}, \tilde{u})_{\Gamma_u^n}, \tag{A.19b}$$
$$-(\Delta t\, k^{-1} q^{n+1}, \tilde{q}) + (\Delta t\, p^{n+1}, \nabla \cdot \tilde{q}) = (\Delta t p_d^{n+1}, \tilde{q} \cdot n)_{\Gamma_p^d}, \tag{A.19c}$$

for all test functions $\tilde{p} \in \mathcal{P}$, $\tilde{u} \in \mathcal{U}_0$, and $\tilde{q} \in \mathcal{Q}_0$. Note that eq. (A.19c) has been multiplied by Δt to maintain symmetry with the term $(\Delta t \nabla \cdot q^{n+1}, \tilde{p})$ in eq. (A.19a).

Appendix A.4. Discretisation in space

For spatial discretization, we employ the mass-conservative three-field finite element formulation (Ferronato et al., 2010) ensuring conservation of mass within the numerical model. The implementation of the finite element formulation (Brenner and Scott, 2008) was carried out using DOLFINx, a finite element computing library (Baratta et al., 2023).

We are guided by Ferronato et al. (2010); Haagenson et al. (2020) in choosing finite element spaces in which the field variables p, u and q are approximated. Specifically, we approximate the pressure $p_h \in \mathcal{P}_h \subset \mathcal{P}$ by zero-order discontinuous Lagrange finite elements, the displacements $u_h \in \mathcal{U}_h \subset \mathcal{U}$ vector-valued first-order continuous Lagrange finite elements, and the flux $q_h \in \mathcal{Q}_h \subset \mathcal{Q}$ the vector-valued Brezzi–Douglas–Marini (BDM) elements (Brezzi et al., 1985) of lowest order which naturally discretise $H(\text{div}; \Omega)$. This formulation is known to be inf-sup stable according to the stability theory of finite element methods (Brenner and Scott, 2008), to guarantee discrete mass conversation (Ferronato et al., 2010), and to be free from spurious pressure oscillations that can cause numerical issues in two-field pressure-displacement formulations of Biot's theory (Ferronato et al., 2010). We note that Ferronato et al. (2010); Alghamdi (2020) use a lowest-order Raviart-Thomas (RT) type space for the flux which has slightly weaker interpolation results than the BDM space used here.

Appendix A.5. Enforcing no normal displacement at well boundary

We briefly describe the method by which we enforce the boundary condition on the normal component of the displacement $u \cdot n = 0$ on the well surface Γ_w as specified in table 4. This boundary condition is recommended as being the most physically justifiable choice in Burbey (2006). By contrast, Alghamdi (2020) did not explicitly include the well surface in their model, instead choosing to model the extraction as a volume forcing using f_p.

Instead of building the boundary condition $u \cdot n = 0$ strongly into the space $\mathcal{U}$, we choose to enforce it weakly using a penalty-free non-symmetric Nitsche-type method proposed in Chouly et al. (2015). Our decision to enforce this condition weakly was made largely to ease the implementation in DOLFINx, where imposing boundary conditions of type $u \cdot n = 0$ strongly in the space is not straightforward.

For simplicity we did not include this more complex boundary condition when developing eq. (A.19), instead choosing to enforce this by a modification to eq. (A.19b) here. Following Chouly et al. (2015) we add two terms on the left-hand side of eq. (A.19b)

$$\begin{aligned} &-(\bar{\sigma}(u^{n+1}, p^{n+1}), \nabla\tilde{u}) \\ &-(\bar{\sigma}(u^{n+1}, p^{n+1}) \cdot n, \tilde{u} \cdot n)_{\Gamma_w} + (\bar{\sigma}(\tilde{u}^{n+1}, \tilde{p}^{n+1}) \cdot n, u \cdot n)_{\Gamma_w} \\ &\qquad = -(f_u^{n+1}, \tilde{u}) - (g_u^{n+1}, \tilde{u})_{\Gamma_u^n}, \quad \forall\tilde{p} \in \mathcal{P}_0, \forall q \in \mathcal{Q}_0. \end{aligned} \tag{A.20}$$

that weakly enforce the condition $u \cdot n = 0$ on Γ_w.

Appendix A.6. Mesh generation

The geometry of the model was meshed using gmsh (Geuzaine and Remacle, 2009) for finite element analysis. The resulting 3D mesh conforms to the the aquifer system's three layers. The element size varies from 6 to 40 m, and the total number of the elements is 368 329. The mesh incorporates different element sizes at different locations and in different layers, this will ensure an appropriate resolution that will improve the accuracy of the model. As we approach the well, the mesh elements become finer, enabling us to the capture of localized effects with lower error.